Modeling the Propagation of Fast Magnetosonic Waves and Their Conversion to Electromagnetic Ion Cyclotron Waves at Low L Shells

Xiang Xu[1], Chen Zhou[1]*, Lunjin Chen[2]* and Richard B. Horne[3]

[1]Department of Space Physics, School of Electronic Information, Wuhan University, Wuhan, China
[2]William B. Hanson Center for Space Sciences, University of Texas at Dallas, Richardson, TX, USA
[3]British Antarctic Survey, Cambridge, UK
Correspondence to:
C. Zhou and L. Chen,
chenzhou@whu.edu.cn; lunjin.chen@gmail.com

Key Points:

- Propagation and mode conversion of fast magnetosonic (MS) to electromagnetic ion cyclotron (EMIC) waves at extremely low L shells is studied with ray tracing and full-wave simulations.
- Right-handedly polarized H^+ band EMIC converted from MS with small (20°) and intermediate (40°) wave normal angles may be efficiently converted to right-handedly polarized He^+ band EMIC or guided left-handedly polarized H^+ band EMIC.
- MS with intermediate (40°) or larger wave normal angles may be efficiently converted to guided left-handedly polarized H^+ band EMIC and the optimal wave normal angles corresponding to the maximum conversion efficiencies decrease with magnetic latitudes.

This article has been accepted for publication and undergone full peer review but has not been through the copyediting, typesetting, pagination and proofreading process, which may lead to differences between this version and the Version of Record. Please cite this article as doi: 10.1029/2022JA031271.

Abstract

The propagation of fast magnetosonic (MS) waves from high to extremely low L shells and their conversion into electromagnetic ion cyclotron (EMIC) waves is investigated with a ray tracing model and a full-wave model. The ray tracing simulations show that MS waves in the vicinity of the local H^+-He^+ crossover frequency at low L shells have a latitudinal range from -20° to 20° with wave normal angles from 0° to 180°, both of which provide the opportunity for their mode conversion to EMIC waves. Results from ray tracing are fed into the full-wave model as initial conditions. The full-wave simulations show that the incoming MS waves with small (20°) and intermediate (40°) wave normal angles may be efficiently converted to right-handedly polarized H^+ band EMIC waves, which may be further converted to right-handedly polarized He^+ band EMIC waves or to guided left-handedly polarized H^+ band EMIC waves through bi-ion resonance reflection and polarization reversal. With intermediate (40°) or larger wave normal angles, via polarization reversal and left-handed polarization cut-off reflection, the incoming MS waves may be efficiently converted to guided left-handedly polarized H^+ band EMIC waves and the optimal wave normal angles corresponding to the maximum conversion efficiencies decrease with magnetic latitudes. Our study verifies the mode conversion mechanism of MS waves to EMIC waves proposed with a previous ray tracing study and examines the dependence of the efficiency of the wave energy transfer on the magnetic latitudes and wave normal angles, which may help to understand the wave properties and distribution of MS and EMIC waves observed at extremely low L shells.

1 Introduction

Fast magnetosonic (MS) waves, also named as equatorial noise (Russell et al., 1970; Gurnett, 1976), are naturally occurring intense electromagnetic emissions and commonly observed from $L = 2$ to $L = 8$ in the magnetosphere (e.g., Perraut et al., 1982; Santolík et al., 2004; Ma et al., 2013). MS waves are often observed within about 10° of the magnetic equator (e.g., Posch et al., 2015; Hrbáčková et al., 2015) but observations beyond this latitudinal range are also reported (e.g., Kasahara et al., 1994; Tsurutani et al., 2014; Zhima et al., 2015). Their frequency range usually extends from local proton cyclotron frequency up to lower hybrid resonance frequency (e.g., Boardsen et al., 1992; Němec et al., 2005; Ma et al., 2013) but MS waves with frequencies below (e.g., Ma et al., 2019; Teng et al., 2019a) or above (e.g., Wu et al., 2021) this range are also observed. MS waves are generally considered to be excited due to unstable ion ring distribution (e.g., Horne et al., 2000; Liu et al., 2011; Min & Liu, 2016) and play an important part in the acceleration (e.g., Horne et al., 2007; Xiao et al., 2015a) and scattering (e.g., Li et al., 2016) of radiation belt energetic electrons.

After excitation, MS waves typically propagate in the whistler mode at the lower-frequency extensions with wave vectors nearly perpendicular to the magnetic field line (e.g., Russell et al., 1970; Gurnett, 1976; Laakso et al., 1990; Stix, 1992; Boardsen et al., 2016). Recent observations (Zou et al., 2019) and simulations (Sun et al., 2020) both show that the power-weighted wave normal angles of MS waves have distributions with peaks a few degrees away from 90°. MS waves can propagate both radially and azimuthally (e.g., Kasahara et al., 1994; Xiao et al., 2012a; Chen & Thorne, 2012; Němec et al., 2013; Santolík et al., 2016; Hanzelka et al., 2022), and across the plasmapause into the plasmasphere when excited outside of the plasmasphere (e.g., Xiao et al., 2015b; Liu et al., 2018; Min et al., 2019). MS waves can further propagate to extremely low L shells ($L < 2.0$) (e.g., Miyoshi et al., 2019; Zhang et al., 2021; Yu et al., 2021) with some even reaching the topside ionosphere observed by DEMETER

(Detection of Electromagnetic Emissions Transmitted from Earthquake Regions) (e.g., Santolík et al., 2016; Němec et al., 2016; Hanzelka et al., 2022). Geomagnetic field strength increases as MS waves propagate toward the Earth and the effects of heavy ions on the propagation start becoming important when the wave frequency becomes lower than the local proton cyclotron frequency. MS waves may go through polarization reversal during inward propagation (e.g., Santolík et al., 2016) and then reflect away from the Earth (e.g., Gurnett & Burns, 1968; Yu et al., 2021).

Electromagnetic ion cyclotron (EMIC) waves can be excited from the ion cyclotron instability due to temperature anisotropy of ring current energetic ions in the equatorial magnetosphere (e.g., Cornwall, 1965; Jordanova et al., 2006; Chen et al., 2010) and their spectra split into multiple bands separated by ion cyclotron frequencies (e.g., Kozyra et al., 1984; Saikin et al., 2015). EMIC waves can be an effective scattering mechanism for the loss of both radiation belt electrons (e.g., Lyons & Thorne, 1972; Usanova et al., 2014; Zhang et al., 2016; Drozdov et al., 2017; Saikin et al., 2022) and ring current ions (e.g., Sakaguchi et al., 2007; Xiao et al., 2012b). Crossover frequency, left-handed polarization (LHP) cut-off frequency and bi-ion resonance frequency are of vital importance for various propagation characteristics of EMIC wave such as polarization reversal, LHP reflection and bi-ion resonance reflection, respectively (e.g., Rauch & Roux, 1982; Hu & Denton, 2009; Chen et al., 2014). The above characteristic frequencies can also affect the mode conversion of EMIC waves. (e.g., Johnson & Cheng, 1999; Hu et al., 2010; Kim & Johnson, 2016; Pakhotin et al., 2022).

Energy of MS waves may be transferred to EMIC waves via various mechanisms. Recently, MS and EMIC waves were observed, simultaneously, at high L shells ($L > 2.0$) (Teng et al., 2019b; Asamura et al., 2021; Zhou et al., 2022) which may be explained by EMIC wave excitation due to superathermal ion anisotropy caused by perpendicular ion heating by MS waves (Asamura et al., 2021; Min et al., 2021). Theoretical studies show that MS waves may be mode converted to EMIC waves near

the magnetic equator (e.g., Lee et al., 2008; Kazakov & Fülüp, 2013; Kim & Johnson, 2014) and at high magnetic latitudes (e.g., Johnson et al., 1995). Mode conversion from MS waves with large wave normal angles to EMIC waves in the equatorial region by branch splitting is possible with the presence of minor heavy ions (D^+ or He^{++}) at extremely low L shells in the plasmasphere (Miyoshi et al., 2019). A ray tracing study performed by Horne and Miyoshi (2016) demonstrates that MS waves with wave normal angles close to 90° outside of the plasmasphere can propagate to extremely low L shells and convert to EMIC waves without attenuation at the crossover frequency when the wave vector of MS wave turns parallel to the geomagnetic field. This proposed linear mode coupling mechanism may explain the observations of MS and EMIC waves with the frequency range of several tens of Hz at overlapped regions by Akebono (Kasahara et al., 1992, 1994). However, only a special case where the parallel propagation of MS and EMIC waves at the crossover frequency is considered in the above ray tracing study and it remains unexplored how likely the condition of the mode conversion can be reached. Furthermore, the ray tracing method is limited in that it does not reveal the physical process of the mode conversion and the efficiency of the energy transfer. To address these questions, we take advantage of the full-wave model developed in this study and ray tracing model IWANE (Investigation of Waves Near the Earth) (Kimura, 1966), to investigate the characteristics of MS waves propagating to extremely low L shells and their linear mode coupling with EMIC waves.

This paper is organized as follows. In Section 2, MS wave properties at extremely low L shells ($L < 2.0$) are obtained based on the ray tracing MS waves originating from high L shells ($L > 2.0$). In Section 3, our full-wave model is introduced and full-wave simulations with results from ray tracing as initial conditions are performed. Simulation results of the wave dynamics during the mode coupling of MS and EMIC waves are presented. Finally, conclusions and discussion of the above simulations and results come in Section 4.

2 Ray Tracing Simulation

The ray tracing program IWANE (Kimura, 1966) is modified to simulate the meridional propagation of MS waves inside the plasmasphere. Diffusive equilibrium cold plasma density model including H^+, He^+, O^+ and electrons (Bortnik et al., 2011) and a dipole magnetic field model are adopted in our simulation. The parameter values of density model and geomagnetic field model used in this paper are the same as in Bortnik et al. (2011).

Since the mode conversion of inward propagating MS waves to EMIC waves likely occurs near the local H^+-He^+ crossover frequency, propagation properties of MS waves there are of great interest and are obtained based on extensive ray tracing simulations. During the simulations, the initial magnetic latitudes λ_0 and the wave frequencies f are fixed at $\lambda_0 = 0^\circ$ and $f = 50$ Hz, respectively, while two other parameters are both sweeping, including the initial wave normal angles θ_{k0} and initial L shells L_0. θ_{k0} varies from 85° to 95° at a step of 0.05° (201 steps) and L_0 varies from 3.05 to 4.5 (the inner edge of plasmapause in our density model) at a step of 0.05 (30 steps), amounting to $201 \times 30 = 6030$ rays launched in our simulations. Statistically most MS waves are observed at $|\lambda| \le 20^\circ$ both at high L shells (Kasahara et al., 1994; Zou et al., 2019) and extremely low L shells (Hanzelka et al., 2022), and only MS waves propagating within this latitudinal range are considered in our ray tracing study. Local H^+-He^+ crossover frequencies increase during the radially inward propagation of MS waves. We terminate ray tracing and switch to full wave simulation at the location where the local H^+-He^+ crossover frequency becomes 47 Hz, about one perpendicular wavelength away from the potential mode conversion region where the local H^+-He^+ crossover frequency matches the wave frequency. Choosing such a terminating location is for the sake of accommodating a directional wave source in the subsequent full-wave simulation in Secion 3. Each ray tracing run is terminated under any of the following three circumstances: (1) the WKB (Wentzel-

Kramers-Brillouin) approximation is violated; (2) the latitude exceeds the range of $|\lambda| \le 20^\circ$; or (3) the local H^+-He^+ crossover frequency exceeds 47 Hz. We only analyze rays with final latitudes λ_1 satisfying $|\lambda_1| \le 20^\circ$ and final local H^+-He^+ crossover frequencies ranging between 47 Hz and 50 Hz. A ray database is obtained through the above ray tracing simulations. All the rays in this database satisfy the above criterions and make up 86.6% of the total 6030 traced rays. The PDFs (probability distribution functions) of final wave normal angles θ_{k1} dependent on the final latitudes λ_1, the initial wave normal angles θ_{k0} and the initial L shells L_0 are calculated from this ray database and demonstrated in Figure 1a, Figure 1b and Figure 1c, respectively.

The PDFs of the final wave normal angles θ_{k1} of the traced rays for different final latitudes λ_1 shown in Figure 1a are divided into 4 subranges according to the deviation from the magnetic equator. Each color indicates a latitudinal subrange and the percentage of the number of rays falling into this subrange is listed. About half of the traced rays terminate close to the latitudinal region $0^\circ \le |\lambda_1| \le 5^\circ$ for which the distribution of θ_{k1} contains a large peak near 90° and extends to about $|\theta_{k1}\text{-}90^\circ| = 60^\circ$. For rays terminated in the latitudinal region $5^\circ < |\lambda_1| \le 20^\circ$, the θ_{k1} of which exhibit distributions with double peaks located away from 90°. The number of rays in each latitudinal subrange decreases with $|\lambda_1|$. The peaks of θ_{k1} distribution for $5^\circ < |\lambda_1| \le 10^\circ$ are centered around $|\theta_{k1}\text{-}90^\circ| = 30^\circ$, shifting to around $|\theta_{k1}\text{-}90^\circ| = 60^\circ$ for $15^\circ < |\lambda_1| \le 20^\circ$. The tails of θ_{k1} distributions for $5^\circ < |\lambda_1| \le 20^\circ$ also indicate the propagation of a non-negligible fraction of MS wave at θ_{k1} within about 30° of the direction parallel (anti-parallel) to the geomagnetic field.

The PDFs of θ_{k1} for various initial wave normal angles θ_{k0} and initial L shells L_0 are presented in a similar format in Figure 1b and Figure 1c, respectively. For θ_{k0} within 1° of the direction perpendicular to the geomagnetic field, the θ_{k1} distribution shows the structure with a single sharp peak centered near 90° and short tails

extending to $\left|\theta_{k1}\text{-}90^{\circ}\right|=30^{\circ}$, as shown in Figure 2b. For $1^{\circ}<\left|\theta_{k0}\text{-}90^{\circ}\right|\le 5^{\circ}$, the θ_{k1} distributions exhibit double peaks and longer tails. As $\left|\theta_{k0}\text{-}90^{\circ}\right|$ increases, the number of rays in each $\left|\theta_{k0}\text{-}90^{\circ}\right|$ subrange decreases and the peaks shift towards larger $\left|\theta_{k1}\text{-}90^{\circ}\right|$. The tails of θ_{k1} distributions for $2^{\circ}<\left|\theta_{k0}\text{-}90^{\circ}\right|\le 5^{\circ}$ can extend to $60^{\circ}<\left|\theta_{k1}\text{-}90^{\circ}\right|<90^{\circ}$. As shown in Figure 1c, the number of rays in each L_0 subrange decreases with increased L_0. The θ_{k1} distributions for $3.0<L_0\le 3.6$ and $3.9<L_0\le 4.5$ show structures with single peaks near 90° while for $3.6<L_0\le 3.9$ the θ_{k1} distribution exhibits three peaks with one around 90° and the other two near $\left|\theta_{k1}\text{-}90^{\circ}\right|=60^{\circ}$. For $3.0<L_0\le 3.6$ and $3.9<L_0\le 4.2$ the θ_{k1} distributions are confined within $\left|\theta_{k1}\text{-}90^{\circ}\right|<60^{\circ}$ while for $3.6<L_0\le 3.9$ and $4.2<L_0\le 4.5$ the tails of the θ_{k1} distribution can extend further to $60^{\circ}<\left|\theta_{k1}\text{-}90^{\circ}\right|<90^{\circ}$.

Three ray tracing cases are selected and the raypaths are plotted with different markers in Figure 1d, in which both axes are normalized by the Earth radius $\mathrm{Re}=6370$ km. The wave normal angles along the raypaths are indicated by colors. As shown in Figure 1d, these rays propagate from high to low L shells in oscillating paths after initiation with their wave normal angles θ_k within $\left|\theta_k\text{-}90^{\circ}\right|<10^{\circ}$ at $L>3.0$. As the rays propagate to $L<3.0$, the deviation of θ_k from 90° becomes much larger and varies rapidly until terminating with local H^{+}-He^{+} crossover frequencies close to 50 Hz (represented by red solid line). In case I, ray launched at $L_0=4.25$ with $\theta_{k0}=93.35^{\circ}$ terminates at $\lambda_1=0^{\circ}$ with $\theta_{k1}=40^{\circ}$ (filled circle); in case II, ray launched at $L_0=4.15$ and $\theta_{k0}=85.95^{\circ}$ terminates at $\lambda_1=20^{\circ}$ with $\theta_{k1}=40^{\circ}$ (empty circle); in case III, ray launched at $L_0=4.15$ and $\theta_{k0}=85.95^{\circ}$ terminates at $\lambda_1=10^{\circ}$ with $\theta_{k1}=110^{\circ}$ (asterisk).

It should be noted that as shown by the results of Figure 1, the probability of the incident MS wave being refracted to be exactly parallel (or anti-parallel) to the geomagnetic field line is very small. The mode conversion from the incident MS wave to EMIC wave can still take place for non-zero wave normal angles. However, the conversion

efficiency should not be 100% anymore and the energy of the converted EMIC wave would be attenuated compared to the incident MS wave. This will be addressed in detail in next section using full-wave simulation.

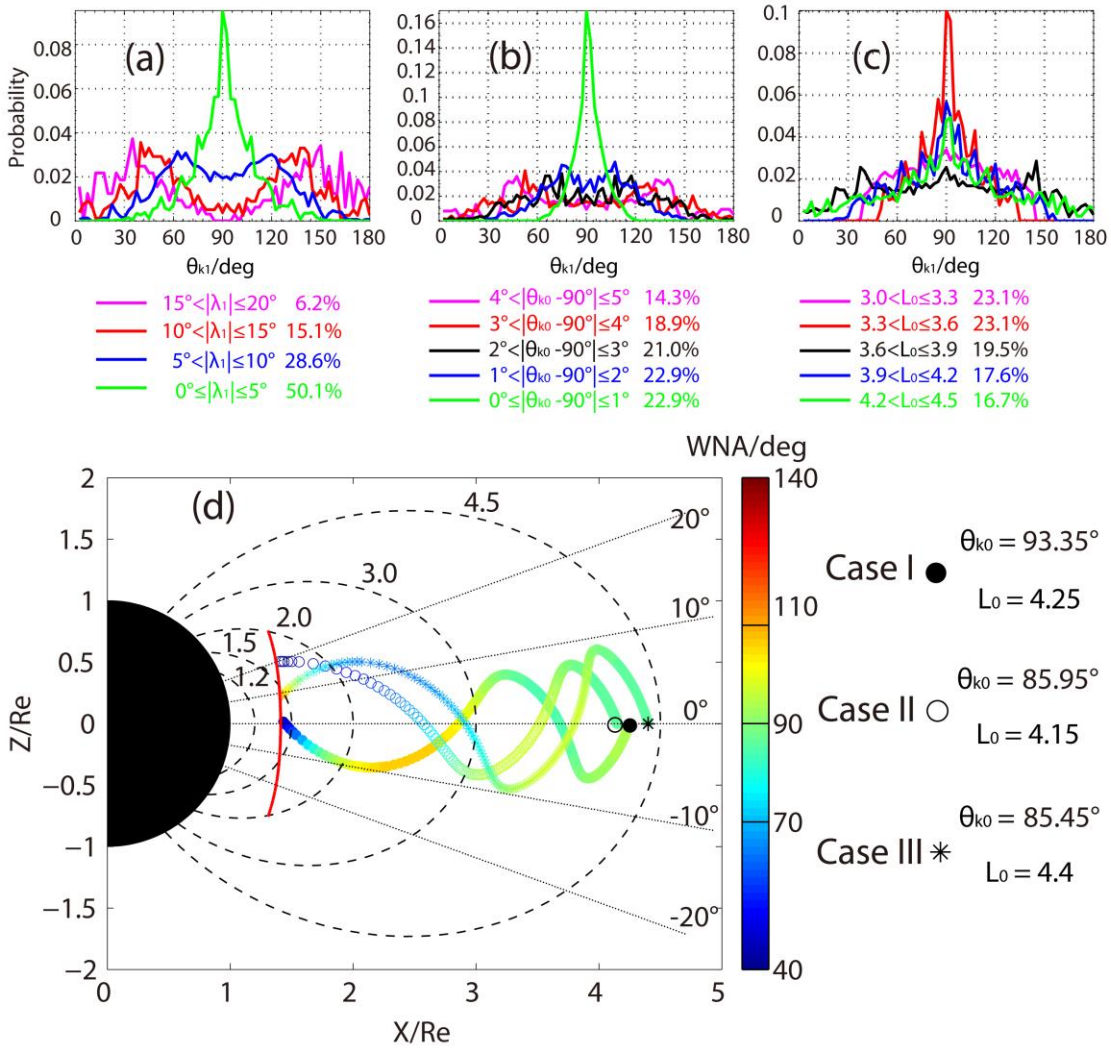

Figure 1. Probability distribution functions of the final wave normal angles θ_{k1} of the traced rays for different (a) final latitudes λ_1, (b) initial wave normal angles θ_{k0} and (c) initial L shells L_0 subranges indicated by colors. (d) Three ray trajectories (labeled with case I, case II and case III respectively) are plotted with different markers and terminating with local H^+-He^+ crossover frequencies close to 50 Hz (marked with the red solid contour) . The wave normal angles along the trajectories during the propagation are indicated by colors.

3 Full-wave Simulation

3.1 Model Description

Our full-wave model is developed to investigate wave propagation in a magnetized and collisional plasma (Xu et al., 2020a). The governing equations include Maxwell's equations coupled with plasma current density equations, presented as follows:

$$\nabla \times \mathbf{E} = -\mu_0 \frac{\partial \mathbf{H}}{\partial t} \tag{1}$$

$$\nabla \times \mathbf{H} = \varepsilon_0 \frac{\partial \mathbf{E}}{\partial t} + \sum\nolimits_{\alpha} \mathbf{J}_{\alpha} \tag{2}$$

$$\frac{\partial \mathbf{J}_{\alpha}}{\partial t} + \upsilon_{\alpha} \mathbf{J}_{\alpha} = \varepsilon_0 \omega_{p\alpha}^2 \mathbf{E} - \boldsymbol{\omega}_{\alpha} \times \mathbf{J}_{\alpha} \tag{3}$$

μ_0 and $\mathbf{H}$ are the vacuum permeability and magnetic field, respectively. ε_0 and $\mathbf{E}$ are the vacuum permittivity and electric field, respectively. $\mathbf{J}_{\alpha}$ represents the plasma current density due to α species including electron, H^+, O^+ and He^+, and υ_{α} is the collision frequency. $\omega_{p\alpha} = \sqrt{n_{\alpha} e^2 / \varepsilon_0 m_{\alpha}}$ is the plasma frequency where n_{α} is the plasma number density, e is the elementary electron charge and m_{α} is the mass of each species. $\boldsymbol{\omega}_{\alpha} = e\mathbf{B}_0 / m_{\alpha}$ is the cyclotron frequency with $\mathbf{B}_0$ the geomagnetic field.

Consider we are interested at the meridional propagation of MS waves at the extremely low L shells and these equations in polar coordinates (r, θ) are solved. $\mathbf{H}$, $\mathbf{E}$ and $\mathbf{J}_{\alpha}$ vectors are obtained from Equation 1, Equation 2 and Equation 3 respectively adopting a Finite-Difference Time-Domain method with a singular update for plasma current density (Pokhrel, Shankar & Simpson, 2018), in which the components of $\mathbf{E}$ and $\mathbf{H}$ are staggered in both time and space (Yee, 1966; Taflove & Hagness, 2005) while the components of $\mathbf{J}_{\alpha}$ are spatially collocated with $\mathbf{E}$ but updated at the same time step as $\mathbf{H}$.

The ratio of the collision frequency, υ_α, to the wave frequency in the inner simulation region is set to zero while increased quadratically by an order of magnitude in all four boundary layers in both r and θ directions, thus imposing artificial absorbing boundary conditions to attenuate the waves propagating in the boundary layers (Streltsov et al., 2006; Xu et al., 2020a).

3.2 Simulation Setup

The parameter values of plasma number density and ambient magnetic field profiles adopted in our full-wave simulation are the same as in Section 2. A two-dimensional spatially Gaussian-shaped wave source is set up to initialize waves with certain polarization and wave normal direction. To impose such directional wave source, three components of $\mathbf{H}$ are used and given in the following forms:

$$\begin{bmatrix} H_{r1}(r,\theta,t) \\ H_{\phi 1}(r,\theta,t) \\ H_{\theta 1}(r,\theta,t) \end{bmatrix} = \exp\left(-\frac{(r-r_1)^2}{\sigma_r^2} - \frac{(\theta-\theta_1)^2}{\sigma_\theta^2} \right) \begin{bmatrix} H_{r1}\sin(k_{r1}r + k_{\theta 1}\theta + 2\pi ft) \\ H_{\phi 1}\cos(k_{r1}r + k_{\theta 1}\theta + 2\pi ft) \\ H_{\theta 1}\sin(k_{r1}r + k_{\theta 1}\theta + 2\pi ft) \end{bmatrix} \quad (4)$$

where $f = 50$ Hz is the wave frequency, (r_1, θ_1) is the center of the wave source, $\sigma_r = 0.0275$ Re and $\sigma_\theta = 0.033$ Re are the half-width of Gaussian distribution. Normalized amplitudes of three $\mathbf{H}$ components (H_{r1}, $H_{\phi 1}$ and $H_{\theta 1}$) and two wave normal vector $\mathbf{k}$ components (k_r and k_θ) are obtained from the cold plasma dispersion of right-handedly polarized whistler mode (Stix, 1992; Swanson, 2003) for given wave frequency f, wave normal angle, local plasma density n_α and geomagnetic field $\mathbf{B}_0$ at (r_1, θ_1) in the simulation region. It should be noted that wave normal angle denotes the angle between $\mathbf{k}$ and the local $\mathbf{B}_0$ in this paper. So firstly we find the solutions of the normalized $\mathbf{H}$ amplitude and $\mathbf{k}$ components in field-aligned coordinates (ψ, χ) where $\nabla\psi/|\nabla\psi|$ is along the field line and $\nabla\chi/|\nabla\chi|$ is perpendicular to $\nabla\psi/|\nabla\psi|$ in the same meridian plane. Then we can obtain their values in polar coordinates through an inverse coordinate transformation

(Kageyama et al., 2006).

Each full-wave simulation run lasts 50 wave periods with a time step of 2.5×10^{-7} s (same for Equations 1-3), with grid spacing of 4.852 km and 0.05° in r and θ direction respectively. The 1200 (r direction) $\times$ 1024 (θ direction) grid is adopted to perform full-wave simulations. The sizes of the lower and upper θ boundary layers are both 1200×100. The size of the upper r boundary layer is 100×1024 while the size of the lower r boundary layer is 50×1024. All components of $\mathbf{E}$, $\mathbf{H}$ and $\mathbf{J}_{\alpha}$ in each computational cell are sampled in time domain. Using these sampled waveforms, wave properties including wave polarization, wave normal angle, Poynting vector and kinetic energy density are obtained for wave propagation analysis. Singular value decomposition method is applied to the sampled $\mathbf{H}$ fields to determine the wave normal angle θ_k and the ellipticity (Santolík et al., 2003).

Both $\mathbf{E}$ and $\mathbf{H}$ fields are used to calculate the Poynting vector $\mathbf{S}$ and its direction θ_s defined as its angle with respect to the local geomagnetic field line, the equations of which are as follows:

$$\mathbf{S} = \frac{1}{T}\int_{t-T}^{t} \mathbf{E}(t)\times\mathbf{H}(t)\,dt \tag{5}$$

$$\theta_s = \arctan\left(\frac{S_{\chi}}{S_{\psi}}\right) \tag{6}$$

where T is the wave period, S_{χ} and S_{ψ} are the perpendicular and field-aligned components of the Poynting vector $\mathbf{S}$ respectively and can be obtained by applying coordinate transformation to the components of $\mathbf{S}$ in polar coordinates. Kinetic energy density E_k is defined with the following equation:

$$E_k = \frac{1}{T}\int_{t-T}^{t} \sum_{\alpha} \frac{m_{\alpha}}{2e^2 n_{\alpha}} \left|\mathbf{J}_{\alpha}(t)\right|^2 dt \tag{7}$$

3.3 Simulation Results

Firstly, we perform full-wave simulation for three cases, whose initial conditions are given by the final latitude λ_1 and the wave normal angle θ_{k1} from the three corresponding cases (case I, II and III) of ray tracing simulation as shown in Figure 1d in Section 2. As shown in Figure 2, local characteristic frequencies are introduced to help illustrate the propagation characteristics of the incident MS wave, including local H^+-He^+ crossover frequency f_{cr1}, LHP cut-off frequency f_{cut1} and bi-ion resonance frequency f_{bi1} and local He^+-O^+ crossover frequency f_{cr2}, LHP cut-off frequency f_{cut2} and bi-ion resonance frequency f_{bi2}. The equations and definitions of these characteristic frequencies are given in Equations A1 - A9 in the Appendix A of Chen et al. (2014). The incident MS wave is located where its wave frequency is slightly higher than f_{cr1}, propagating as right-handedly polarized whistler (R1) (Figure 2a). Possible wave modes into which incident MS waves can convert (or evolve) during its inward propagation are shown in Figure 2b, including right-handedly polarized H^+ band EMIC wave (R2) (He^+ band EMIC wave if $\omega/\omega_{cH^+} < 0.25$) between f_{cr1} and f_{cr2}, right-handedly polarized He^+ band EMIC wave (R3) below f_{cr2}, unguided left-handedly polarized H^+ band EMIC wave (L1) between f_{cut1} and f_{cr1}, guided left-handedly polarized H^+ band EMIC wave (L2) between f_{cr1} and H^+ cyclotron frequency, unguided left-handedly polarized He^+ band EMIC wave (L3) between f_{cut2} and f_{cr2} and guided left-handedly polarized He^+ band EMIC wave (L4) between f_{cr2} and He^+ cyclotron frequency.

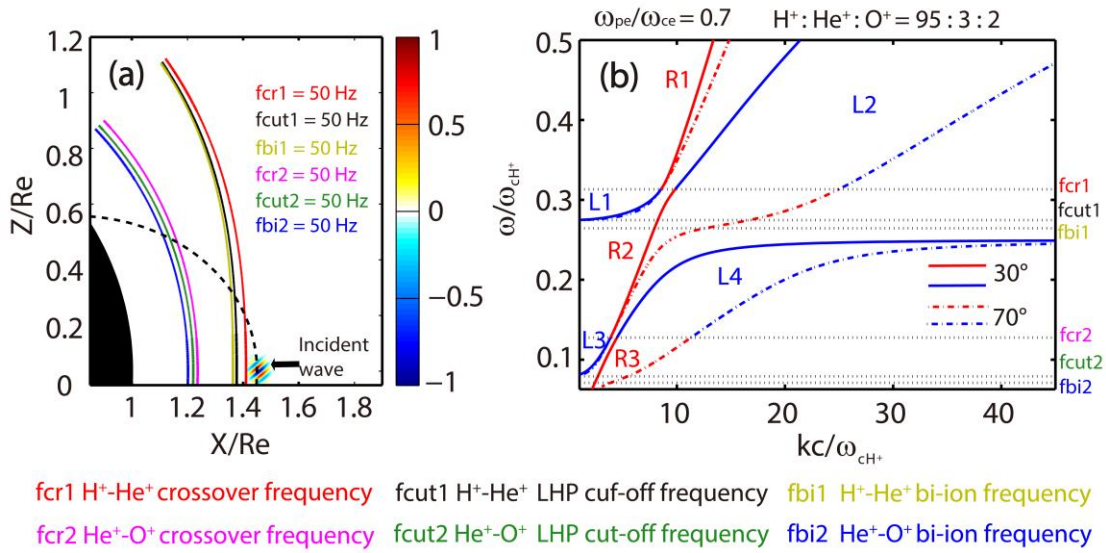

Figure 2. (a) Radial component of the directional wave source with normalized amplitude located at the magnetic equator at $t = 0$. Contours of various colors denote where the local characterestic frequencies match the wave frequency of 50Hz. The dashed curve through the wave source represents the geomagnetic field line at $L = 1.45$. (b) Dispersion curves for waves propagating at $\theta_k = 30^\circ$ (solid curves) and $\theta_k = 70^\circ$ (dashed curves) with typical plasma parameters in the simulation domain. Red and blue curves represent right-handed and left-handed polarization respectively and joined at crossover frequencies in the same branch. Various wave modes are labeled with R1-R3 and L1-L4.

Results of the full-wave simulation runs of the three cases are presented in Figures 3-5, respectively, which demonstrate the feasibility of the mode conversion between the incident MS waves and the EMIC waves.

In case I, the simulation domain covers the radial range from 1.12 Re to 1.9 Re and the latitudinal range from -10° to 50°. The MS wave incident from the magnetic equator ($\lambda_1 = 0^\circ$ and $r_1 = 1.4567$ Re) with $\theta_{k1} = 40^\circ$ and right-handed polarization propagates towards higher latitudes with θ_k slowly decreasing to 30° near f_{cr1}, as presented in Figure 3k. As the incident wave (R1) encounters f_{cr1}, both mode coupling

and polarization reversal take place. One portion is converted to a right-handedly polarized H^+ band EMIC wave (R2) (Figure 3c and Figure 3i) and tunneled through f_{cr1} and f_{bi1} to lower L shells. The other portion reverses its polarization and propagates as a left-handedly polarized whistler (L1) (Figure 3i), which reflects at f_{cut1} indicated by the increase of kinetic energy density between f_{cut1} and f_{cr1} (Figure 3h), then changes its polarization back to right-handed (R1) at f_{cr1} (Figure 3i). The right-handedly polarized H^+ band EMIC wave (R2) splits at f_{cr2} and a small portion with θ_k around 20° (Figure 3g and Figure 3k) is further converted to a right-handedly polarized He^+ band EMIC wave (R3) (Figure 3c and Figure 3i). The other portion reflects back and still propagates as a right-handedly polarized H^+ band EMIC wave (R2). The wave (R2) increases its θ_k rapidly to 90° (Figure 3k), experiences bi-ion resonance reflection indicated by the enhancement of kinetic energy density around f_{bi1} (Figure 3h) then decreases its θ_k to the lower value about 60° (Figure 3k) when approaching f_{bi1}. Upon crossing f_{cr1}, the wave (R2) reverses its polarization and propagates as a guided left-handedly polarized H^+ band EMIC wave (L1) (Figure 3i) towards larger L shells and lower latitudes along the field line (Figure 3j), which is consistent with the ray tracing case in Horne and Miyoshi (2016).

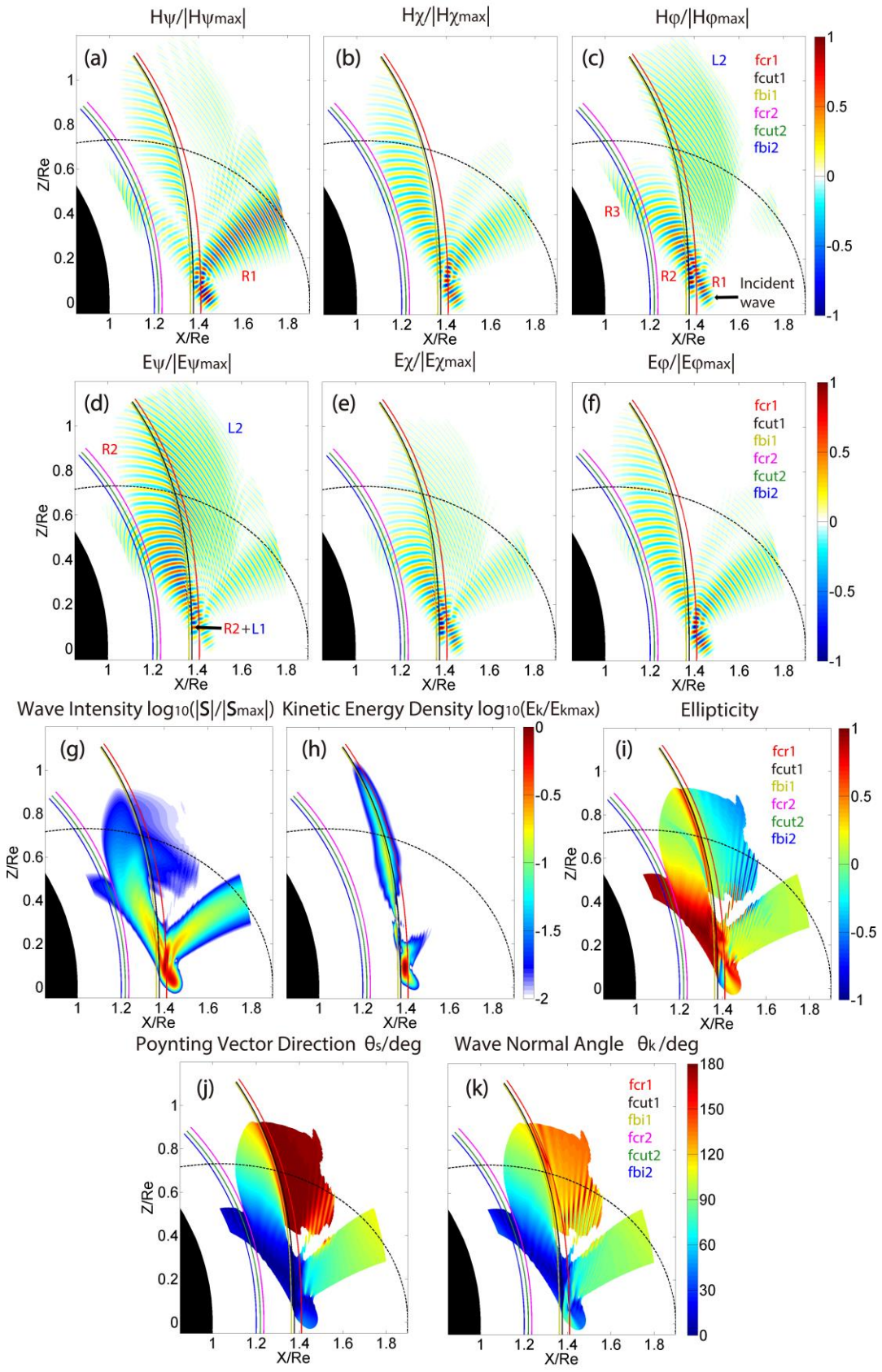

Figure 3. Propagation characteristics of the MS wave incident from the magnetic equator with the initial wave normal angle $\theta_{k1} = 40^{\circ}$ (case I). (a)-(f) Profiles of

magnetic and electric field components in field-aligned coordinates with normalized amplitudes: $\frac{H_\psi}{|H_{\psi\max}|}$, $\frac{H_\chi}{|H_{\chi\max}|}$, $\frac{H_\varphi}{|H_{\varphi\max}|}$, $\frac{E_\psi}{|E_{\psi\max}|}$, $\frac{E_\chi}{|E_{\chi\max}|}$ and $\frac{E_\varphi}{|E_{\varphi\max}|}$, respectively. φ denotes the azimuthal direction. Wave modes including R1-R3, L1 and L2 are labeled. (g)-(h) Normalized wave intensity $\log_{10}\left(\frac{|\mathbf{S}|}{|\mathbf{S}_{\max}|}\right)$ and kinetic energy density $\log_{10}\left(\frac{E_k}{E_{k\max}}\right)$, respectively. (i) Ellipticity. 1 (-1) indicates purely right-handed (left-handed) circular polarization and 0 indicates linear polarization. (j)-(k) Poynting vector direction θ_s and wave normal angle θ_k. 0° (180°) indicates the direction parallel (anti-parallel) to the local geomagnetic field line. The dashed curve in each subfigure represents the geomagnetic field line at $L = 1.9$.

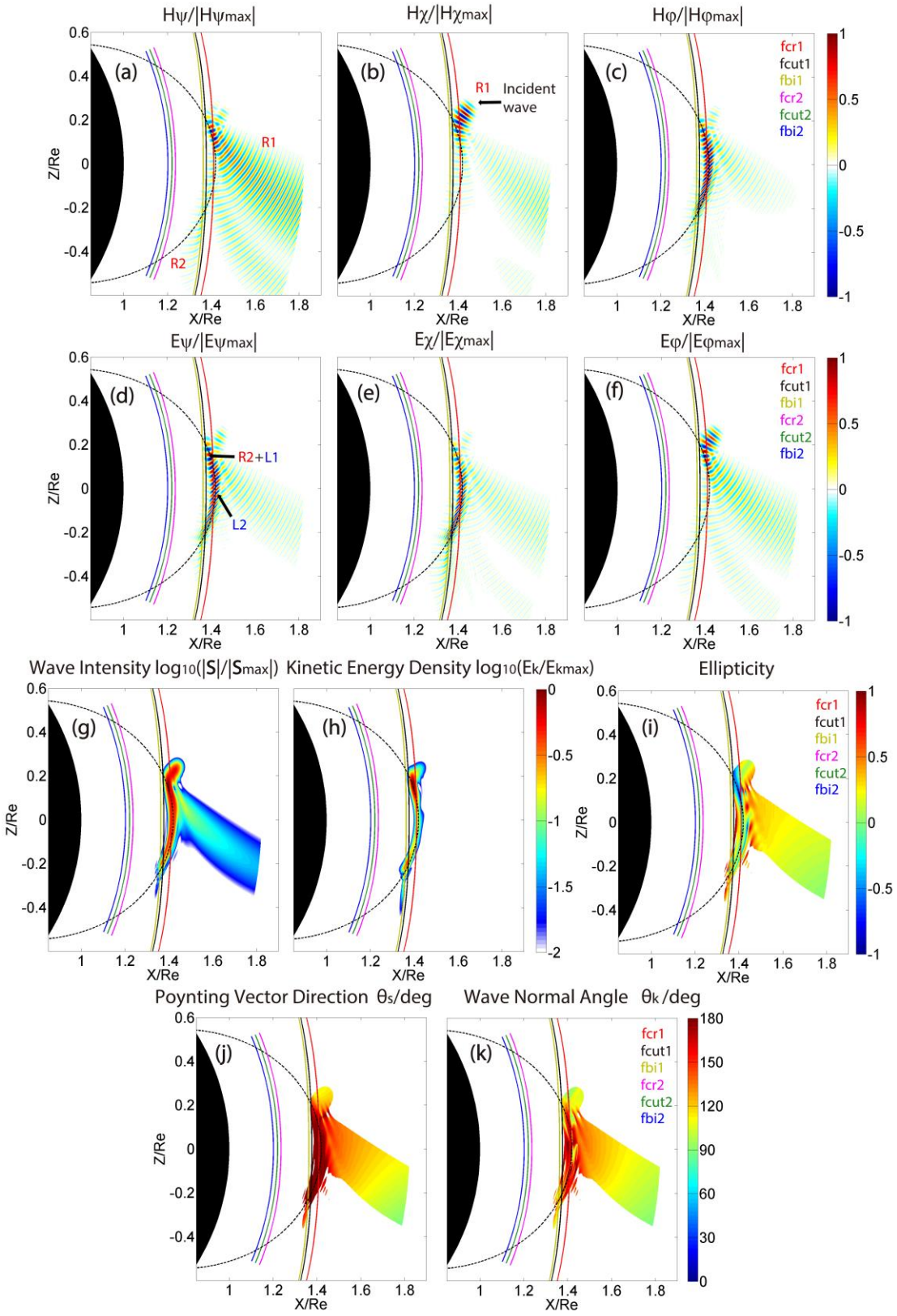

Figure 4. Propagation characteristics of the MS wave incident from $\lambda_1 = 10^\circ$ with the initial wave normal angle $\theta_{k1} = 110^\circ$ (Case II). (a)-(f) Profiles of magnetic and electric

field components in field-aligned coordinates with normalized amplitudes: $\frac{H_\psi}{|H_{\psi\max}|}$, $\frac{H_\chi}{|H_{\chi\max}|}, \frac{H_\varphi}{|H_{\varphi\max}|}, \frac{E_\psi}{|E_{\psi\max}|}, \frac{E_\chi}{|E_{\chi\max}|}$ and $\frac{E_\varphi}{|E_{\varphi\max}|}$, respectively. Wave modes including R1, R2, L1 and L2 are labeled. (g)-(h) Normalized wave intensity $\log_{10}\left(\frac{|\mathbf{S}|}{|\mathbf{S}_{\max}|}\right)$ and kinetic energy density $\log_{10}\left(\frac{E_k}{E_{k\max}}\right)$, respectively. (i) Ellipticity. (j)-(k) Poynting vector direction θ_s and wave normal angle θ_k. The dashed curve in each subfigure represents the geomagnetic field line at L= 1.42.

In case II, the simulation domain covers the radial range from 1.12 Re to 1.9 Re and the latitudinal range from -30° to 30°. The linearly polarized MS wave incident from $\lambda_1 = 10^\circ$ and r_1 = 1.4696 Re with $\theta_{k1} = 110^\circ$ propagates towards lower latitudes, as shown in Figure 4. The wave energy splits at f_{cr1} with only a small portion converted to a right-handedly polarized H^+ band EMIC wave (R2) (Figure 4a and Figure 4g). The subsequent propagation of this mode-converted EMIC wave (R2) is similar to case I shown in Figure 3, except its crossing the equator. A very large portion of the incident wave changes its polarization to left-handed upon crossing f_{cr1} (Figure 4g and Figure 4i). During its reflection at f_{cut1} (Figure 4h), the left-handedly polarized whistler (L1) varies its θ_k to about 150° (Figure 4k) and starts to propagate towards f_{cr1}. When the wave (L1) encounters f_{cr1}, most of the wave energy is converted to a guided left-handedly polarized H^+ band EMIC wave (L2) while a small portion of the wave (L1) reverses its polarization and propagates away from the Earth as a right-handedly polarized whistler (R1) (Figure 4a and Figure 4d). The guided left-handedly polarized H^+ band EMIC wave (L2) continues its field-aligned propagation across the equator and to the southern hemisphere (Figure 4j) with its θ_k increased until its second encounter with f_{cr1} and reflection near f_{bi1} and f_{cut1} (Hu et al., 2010; Kim & Johnson, 2016; Pakhotin et al., 2022) .

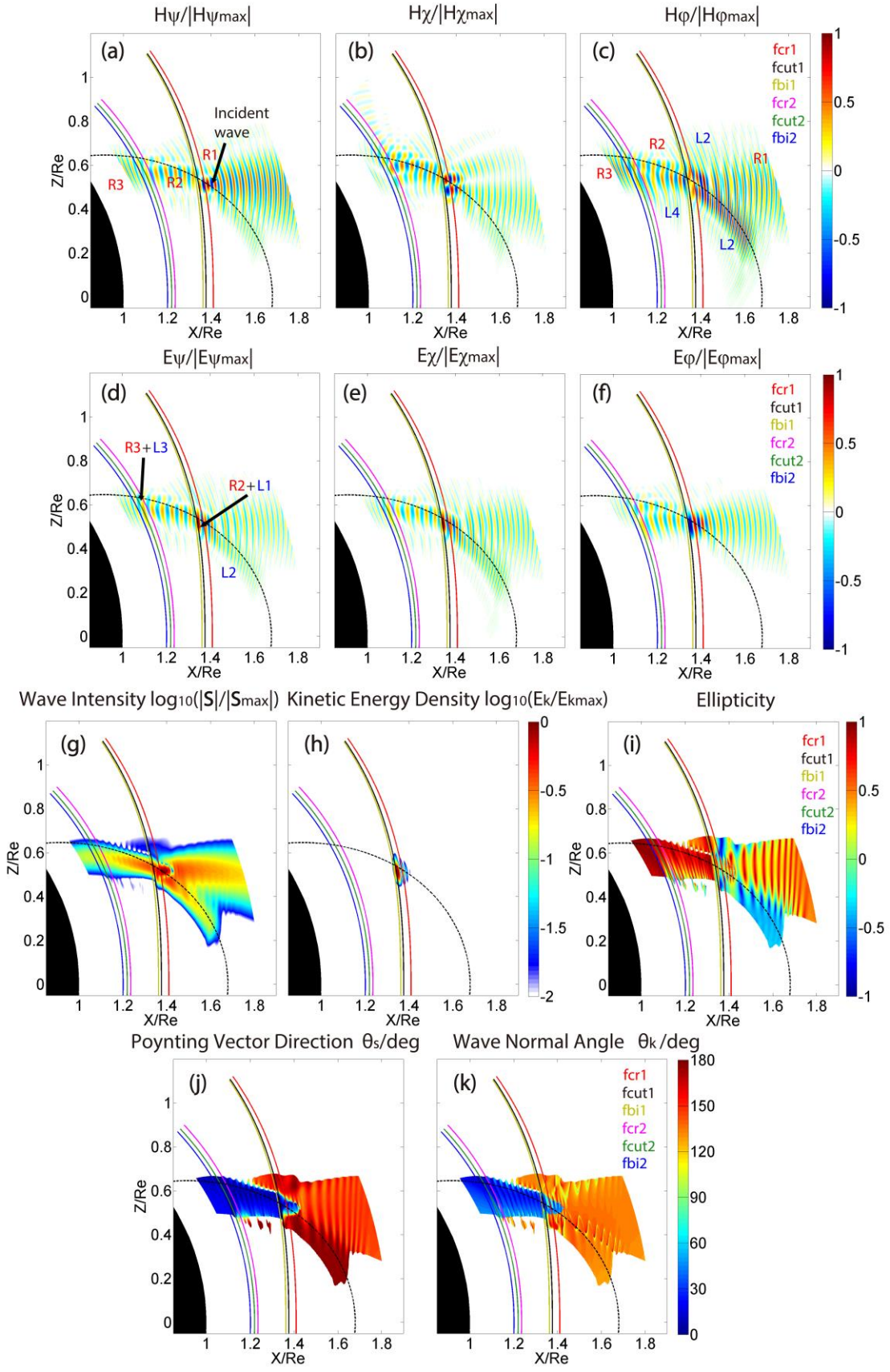

Figure 5. Propagation characteristics of the MS wave incident from $\lambda_1 = 20^\circ$ with the

initial wave normal angle $\theta_{k1} = 40^{\circ}$. (a)-(f) Profiles of magnetic and electric field components in field-aligned coordinates with normalized amplitudes: $\frac{H_{\psi}}{|H_{\psi\max}|}$, $\frac{H_{\chi}}{|H_{\chi\max}|}$, $\frac{H_{\varphi}}{|H_{\varphi\max}|}$, $\frac{E_{\psi}}{|E_{\psi\max}|}$, $\frac{E_{\chi}}{|E_{\chi\max}|}$ and $\frac{E_{\varphi}}{|E_{\varphi\max}|}$, respectively. Wave modes including R1-R3 and L1-L4 are labeled. (g)-(h) Normalized wave intensity $\log_{10}\left(\frac{|\mathbf{S}|}{|\mathbf{S}_{\max}|}\right)$ and kinetic energy density $\log_{10}\left(\frac{E_k}{E_{k\max}}\right)$, respectively. (i) Ellipticity. (j)-(k) Poynting vector direction θ_s and wave normal angle θ_k. The dashed curve in each subfigure represents the geomagnetic field line at L= 1.68.

In case III, the spatial range of the simulation domain is the same as in case I. The MS wave with $\theta_{k1} = 40^{\circ}$ and right-handed polarization is incident from $\lambda_1 = 20^{\circ}$ and r_1 = 1.5153 Re, propagating towards higher latitudes, as presented in Figure 5. The incident wave (R1) splits at f_{cr1} due to the mode conversion and polarization reversal at the same time. One portion propagates as a left-handedly polarized whistler (L1) due to polarization reversal, reflects back at f_{cut1} (Figure 5h) and approaches f_{cr1} again. The wave (L1) splits into two portions at f_{cr1} with one reversing its polarization back to the right-handed polarization mode (R1) and the other converted to a guided left-handedly polarized H^+ band EMIC wave (L2) propagating towards the magnetic equator along the field line (Figure 5c, Figure 5d and Figure 5j). The other portion from the incident wave (R1) is converted to a right-handedly polarized H^+ band EMIC wave (R2) and propagating towards f_{cr2} (Figure 5a and Figure 5c). Similar to the propagation near f_{cr1}, the wave (R1) eventually splits into 3 portions at f_{cr2}. Most of the wave energy is tunneled to lower L shells as a right-handedly polarized He^+ band EMIC wave (R3) (Figure 5a and Figure 5c). The reflected portions include a guided left-handedly polarized He^+ band EMIC wave (L3) and a right-handedly polarized H^+ band EMIC wave (R2) that propagates as a guided left-handedly polarized H^+

band EMIC wave (L2) upon its crossing f_{cr1} (Figure 5c, Figure 5d and Figure 5i). The mode conversion from the incident MS wave to different modes of EMIC waves in this case is similar to the linear mode conversion from whistler mode waves to ion cyclotron mode waves at high latitudes discussed in both theoretical (Johnson et al., 1995) and simulation (Xu et al., 2020b) studies.

Finally, the dependence of mode conversion of the incoming MS wave on the initial magnetic latitudes λ_1 and wave normal angles θ_{k1} is investigated using full-wave simulations with various combinations of λ_1 and θ_{k1}. Specifically, the efficiencies of the mode conversion to the right-handedly polarized H^+ band EMIC wave (R2 mode), the guided left-handedly polarized H^+ band EMIC wave (L2 mode) and the right-handedly polarized He^+ band EMIC wave (R3 mode) are analyzed based on the results presented in Figure 6.

When the incoming MS wave (R1 mode) is from the magnetic equator ($\lambda_1 = 0^\circ$) with small θ_{k1} (20°) (Figure 6a) and intermediate θ_{k1} (40°) (Figure 6b), the mode conversion from the R1 mode to L2 mode is through the propagation path presented in Figure 3 and dependent on the bi-ion resonance reflection and polarization reversal of the R2 mode converted from R1 mode before, which is defined as Path A in this paper. As shown in Figure 6a and Figure 6l, a significant portion of the incident R1 mode with small θ_{k1} (or $180^\circ - \theta_{k1}$) may be unable to access the mode conversion region due to the effects of the magnetic curvature, thus reducing the mode conversion efficiency from the R1 mode to R2 mode with such initial wave normal angles. Meanwhile, the wave intensity of the converted R2 mode decreases with the increasing θ_{k1} from an intermediate value (40°) to large values (60° and 80°) at different λ_1 as shown in Figures 6b-6d, Figures 6f-6h and Figures 6n-6p, respectively. The above dependence of the mode conversion efficiency on the variation of θ_{k1} indicates that an optimal initial wave normal angle $\theta_{L2\text{PathA}}$ exists, with which the efficiency of mode conversion from the R1 mode to L2 mode through the Path A may reach its maximum.

At $\lambda_1 = 0^\circ$, the $\theta_{L2\text{PathA}}$ is around 40° (Figure 6b). As the incident λ_1 increases to $\lambda_1 = 10^\circ$, the $\theta_{L2\text{PathA}}$ decreases to around 20° (Figure 6e). With λ_1 increased to $\lambda_1 = 20^\circ$, the mode conversion from the R1 mode to L2 mode through the Path A becomes much less efficient (Figure 6m) compared to the cases at $\lambda_1 = 10^\circ$ and $\lambda_1 = 0^\circ$. The propagation path through which R1 mode is mode converted to L2 mode presented in Figure 4 is defined as Path B. This mode conversion to L2 mode is dependent on the LHP cut-off reflection of the L1 mode resulted from the polarization reversal of the incident R1 mode and it is more efficient off the magnetic equator as shown in Figure 6. At $\lambda_1 = 10^\circ$, the L2 mode converted from R1 mode starts to appear with large θ_{k1} (80°) (Figure 6h). The wave intensity of L2 mode increases as θ_{k1} is increased from 80° to 110° (Figures 6h-6j) then decreases as θ_{k1} is decreased from 110° to 150° (Figures 6j-6l), indicating the existence of an optimal initial wave normal angle $\theta_{L2\text{PathB}}$ around 110°. At $\lambda_1 = 20^\circ$, the L2 mode starts to appear around an intermediate θ_{k1} (40°) (Figure 6n) and its wave intensity increases as θ_{k1} is increased from 40° to 80° (Figures 6n-6p). With θ_{k1}=80°, most of the wave energy of the R1 mode is transferred to L2 mode through Path B, indicating the $\theta_{L2\text{PathB}}$ is around 80° at $\lambda_1 = 20^\circ$. Moreover, $\theta_{L2\text{PathB}}$ decreases with λ_1 based on the comparison between the cases at $\lambda_1 = 10^\circ$ and $\lambda_1 = 20^\circ$ shown in Figure 6.

Similar to the mode conversion from the R1 mode to L2 mode through Path A, the conversion from the R1 mode to R3 mode is also dependent on the R2 mode converted from R1 mode before and it tends to occur for small (20°) and intermediate (40°) θ_{k1}. At the magnetic equator, an optimal initial wave normal angle for the conversion to R3 mode exists and it is around 40° (Figure 6b). Off the magnetic equator, the mode conversion to R3 mode is more effective than the equatorial cases and the wave intensity of the R3 mode keeps decreasing with θ_{k1} till it becomes insignifant in our simulation at $\lambda_1 = 10^\circ$ (Figures 6e-6h) and $\lambda_1 = 20^\circ$ (Figures 6m-6p).

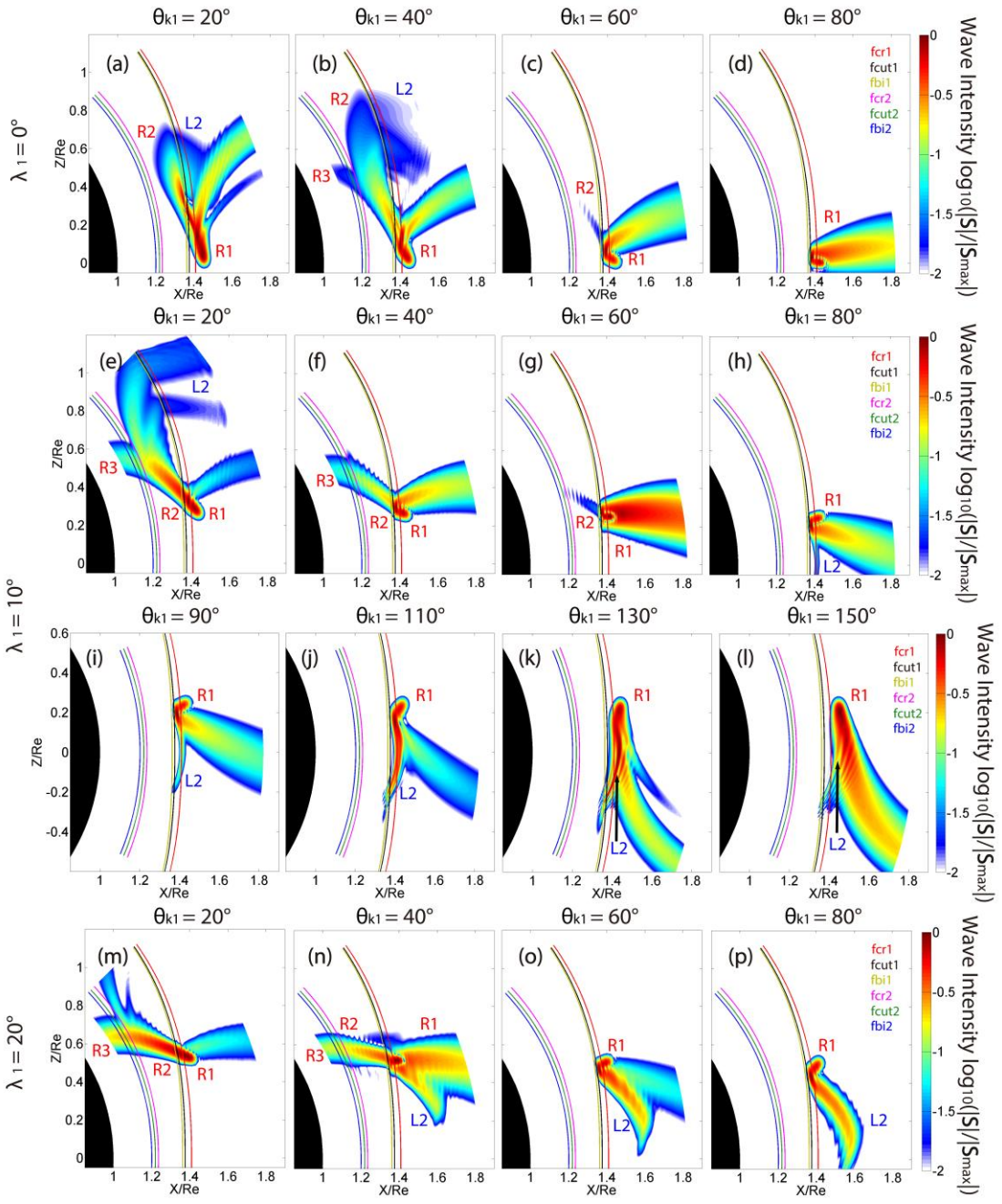

Figure 6. Spatial distributions of normalized wave intensity for incoming waves (R1) from magnetic latitudes (a)-(d) $\lambda_1 = 0^\circ$, (e)-(l) $\lambda_1 = 10^\circ$ and (m)-(p) $\lambda_1 = 20^\circ$ respectively with various initial wave normal angles θ_{k1} after mode conversion. Different wave modes including R1-R3 and L2 are labeled in subfigures accordingly.

4 Conclusions and Discussion

The propagation of MS waves to extremely low L shells and their conversion to EMIC

waves is modeled by ray tracing and full-wave simulations in this study. Ray tracing is used to simulate the propagation of MS waves from high L shells ($L > 2.0$), in which rays initiate with various wave normal angles θ_{k0} at various initial L shells L_0 and terminate at low L shells ($L < 2.0$) where the wave frequency is close to the local H^+-He^+ crossover frequency (f_{cr1}). The final latitudes λ_1 and wave normal angles θ_{k1} from ray tracing are into the full-wave model we developed in this study as the initial conditions of full-wave simulations where the propagation of MS waves and their mode coupling with EMIC waves near the local characteristic frequencies are modeled. Principle conclusions drawn from the results of ray tracing and full-wave simulations are summarized as follows:

1. MS waves with θ_{k0} ranging from 85° to 95° at the magnetic equator and high L shells may propagate to the vicinity of f_{cr1} at low L shells, where they have final latitudes λ_1 ranging from -20° to 20° with final wave normal angles θ_{k1} ranging from 0° to 180°. Through the local characteristic frequencies, they may be mode converted to right-handedly polarized H^+ band EMIC waves (R2 mode), He^+ band EMIC waves (R3 mode) and guided left-handedly polarized H^+ band EMIC waves (L2 mode), which supports the suggestion put forward by Horne and Miyoshi (2016).

2. Two potential propagation paths are presented through which the incoming MS wave (R1 mode) may be converted to L2 mode. The bi-ion resonance reflection and polarization reversal of the R2 mode converted from R1 mode before are essential during the Path A (Figure 3). The mode conversion to L2 mode is more efficient with small (20°) and intermediate (40°) θ_{k1} at λ_1 within $\pm 10^\circ$ for Path A. The LHP cut-off reflection of L1 mode resulted from the polarization reversal of the incident R1 mode is important during the Path B (Figure 4). The mode conversion to L2 mode is more efficient with intermediate (40°) or larger θ_{k1} at λ_1 higher than $\pm 10^\circ$ for Path B. The optimal initial wave normal angle for the mode conversion to L2 mode during the Path B decreases with λ_1.

3. The incoming MS wave may also be converted to R3 mode, which tends to occur for small (20°) and intermediate (40°) θ_{k1} and is more efficient off the magnetic equator at $\lambda_1 = 10^\circ$ or higher magnetic latitudes.

Both ray tracing and full-wave simulation in this study are confined on a fixed meridian plane and the azimuthal propagation of MS waves is not considered. Previous ray tracing studies have shown that MS waves inside the plasmasphere over 100 Hz can propagate to the altitude of low Earth orbit satellites, such as DEMETER, only when the initial azimuthal deviation from the radial direction is extremely small (within a few degrees or even less) (Santolík et al., 2016, Hanzelka et al., 2022) while MS waves with frequency lower than 100Hz may reach $L < 2.0$ with the initial azimuthal deviation below 30° (Kasahara et al., 1994; Chen & Thorne, 2012). The contribution of the azimuthal propagation to the wave behavior during the mode conversion at extremely low L shells and subsequent propagation of the reflected MS waves need to be dealt with 3D ray tracing model and full-wave model.

θ_{k0} of MS waves are assumed to have a uniform distribution from 85° to 95° in our ray tracing and all rays are launched from exactly the magnetic equator. These two assumptions may have resulted in the sharp peaks of the θ_{k1} distributions around 90° (Hanzelka et al., 2022) in our study and observations of MS waves at $L < 2.0$ are needed to obtain realistic θ_{k1} distributions that are crucial to the propagation characteristics of MS wave below local proton cyclotron frequency and the potential mode conversion.

Statistical investigation (Zou et al., 2019) shows that power-weighted wave normal angles of MS waves at $2.0 < L < 6.0$ are dominantly within 87° to 89° near the equatorial region ($|\lambda_1| \le 5^\circ$). Particle-in-cell simulation (Sun et al., 2020) finds that power-weighted wave normal angles of MS waves range from 82° to 89° during the

linear growth but increase to within 84° to 89° during saturation. It is noteworthy that the small and intermediate population of the θ_{k1} distribution will increase while the population of large θ_{k1} will decrease if we adopt the wave normal angles from the above studies as the initial conditions of our ray tracing, suggesting the efficiency of the mode conversion presented in our full-wave simulation should be higher.

In our full-wave simulation the incident MS wave cannot be assumed as a pure plane wave with the intended wave normal angle θ_{k1} as shown in Figures 3-6, although a directional wave source is adopted. The incident wave from the edge of the Gaussian-shaped wave source may propagate with wave normal angle significantly deviating from the intended value (e.g., Figure 3k), which also contributes to the overall wave behavior near the local characteristic frequencies. Proper parameters of Gaussian half-widths are used in our study so that the wave normal angle of the incident wave from the interior of the wave source is much closer to the intended value than the edge of the wave source (e.g., Figure 3k). Moreover, the intensity of the incident wave from the interior of the wave source is much larger than the edge of the wave source (e.g., Figure 3g), so that the mode conversion and the spatial distribution of the wave energy near the local characteristic frequencies are mostly determined by the incident MS wave from the interior of the wave source. This is also consistent with the dependence of the propagation paths and mode conversion efficiency of the incident MS wave on the intended wave normal angle θ_{k1} as shown in Figure 6. Whether the size of the wave source in our full-wave simulation represents the real situation of the MS wave in the magnetosphere may be confirmed with multi-point measurements, which is out of the scope of this paper.

As has been mentioned in Section 2 and Section 3, the parameters of the propagation medium are the same as in Bortnik et al. (2011) with the ratio of electron plasma frequency to cyclotron frequency ω_{pe}/ω_{ce} about 0.7 and 2-3% He^+ in ion composition in the vicinity of the local H^+-He^+ crossover frequency while ω_{pe}/ω_{ce}

is around 3.3 and the concentration of He^+ is around 7% in Horne and Miyoshi (2016). The consistency of the mode conversion paths in our study with Horne and Miyoshi (2016) suggests that linear mode coupling of MS and EMIC waves may occur for a relatively wide range of ambient plasma conditions at low L shells. Previous theoretical studies show that the tunneling from the incident R1 mode to R2 mode (or further to R3 mode) near the characteristic frequencies is dependent on the concentration of the minor ions (He^+ or O^+ in our case) and the efficiency of the tunneling decreases with the concentration of the minor ion and the wave normal angle (Johnson et al., 1995; Lee et al., 2008; Kazakov & Fülüp, 2013; Kim & Johnson, 2014). The propagation of the guided left-handedly polarized EMIC wave near the characteristic frequencies is also discussed in some studies, which show that the guided L mode EMIC wave may be tunneled through the bi-ion resonance frequency with a lower concentration of the minor ion (Hu et al., 2010) or reflect near the bi-ion frequency with a higher concentration of the minor ion (Khazanov et al., 2006). The tunneling efficiency should depend on both the wave properties and the plasma medium (Perraut et al., 1984; Johnson et al., 1995; Johnson & Cheng, 1999; Khazanov et al., 2006; Hu et al., 2010). If the wave-particle interaction is considered, the guided L mode EMIC may also be subject to the ion cyclotron absorption at the bi-ion frequency (Thorne & Horne, 1993; Hu et al., 2010) and the second harmonic of the cyclotron frequency of the minor ion (Horne & Thorne, 1990; Hu et al., 2010) or the electron landau damping with large wave normal angles after the bi-ion resonance reflection (Kasahara et al., 1992; Thorne & Horne, 1992; Khazanov et al., 2007). In our case, only cold plasma is considered and the He^+ concentration is about 2-3% near the characteristic frequencies as mentioned above, most of the wave energy of the converted L2 mode from the incident R1 mode reflects near the bi-ion frequency, similar to the propagation of the guided L mode He^+ band EMIC wave with its wave normal angle of $\sim 50^\circ$ and its wave vector pointing away from the Earth as simulated in Kim & Johnson (2016). The local characteristic frequencies are dependent on the composition of heavy ions (Chen et al., 2014) and the spatial variation of heavy ions of different species (Matsuda et al., 2016; Miyoshi et al.,

2019) can modify the location of these characteristic frequencies. It is left as a future study how the ion composition may affect the energy distribution of different wave modes due to mode conversion.

Data Availability Statement

Data from full-wave simulation and ray tracing in this study are available at https://doi.org/10.5281/zenodo.7875579
The IWANE (Ray tracing program for Investigation of WAves Near the Earth) is available at http://space.rish.kyoto-u.ac.jp/software/IWANE_src.zip.

Acknowledgement

This research is supported by National Natural Science Foundation of China (NSFC) (Grants NO. 42104149).

References

Asamura, K., Shoji, M., Miyoshi, Y., Kasahara, Y., Kasaba, Y., Kumamoto, A., et al. (2021). Cross-energy couplings from magnetosonic waves to electromagnetic ion cyclotron waves through cold ion heating inside the plasmasphere. *Physical Review Letters*, **127**, 245101. https://doi.org/10.1103/PhysRevLett.127.245101
Boardsen, S. A., Gallagher, D. L., Gurnett, D. A., Peterson, W. K., & Green, J. L. (1992). Funnel-shaped, low-frequency equatorial waves. *Journal of Geophysical Research: Space Physics*, **97**(A10), 14967–14976. https://doi.org/10.1029/92JA00827
Boardsen, S. A., Hospodarsky, G. B., Kletzing, C. A., Engebretson, M. J., Pfaff, R. F., Wygant, J. R., et al. (2016). Survey of the frequency dependent latitudinal distribution of the fast magnetosonic wave mode from Van Allen Probes electric and magnetic field instrument and integrated science waveform receiver plasma wave analysis. *Journal of Geophysical Research: Space Physics*, **121**, 2902– 2921. https://doi.org/10.1002/2015JA021844
Bortnik, J., Chen, L., Li, W., Thorne, R. M., & Horne, R. B. (2011). Modeling the evolution of chorus waves into plasmaspheric hiss. *Journal of Geophysical Research: Space Physics*, **116**(A8). https://doi.org/10.1029/2011JA016499
Chen, L., Thorne, R. M., Jordanova, V. K., Wang, C.-P., Gkioulidou, M., Lyons, L., & Horne, R. B. (2010). Global simulation of EMIC wave excitation during the 21 April 2001 storm from coupled RCM-RAM-HOTRAY modeling. *Journal of Geophysical Research: Space Physics*, **115**(A7), 7209. https://doi.org/10.1029/2009JA015075
Chen, L., & Thorne, R. M. (2012). Perpendicular propagation of magnetosonic waves. *Geophysical Research Letters*, **39**, L14102. https://doi.org/10.1029/2012GL052485
Chen, L., Jordanova, V. K., Spasojevic, M., Thorne, R. M., & Horne, R. B. (2014).

Electromagnetic ion cyclotron wave modeling during the geospace environment modeling challenge event. *Journal of Geophysical Research: Space Physics*, **119**, 2963–2977. https://doi.org/10.1002/2013JA019595

Cornwall, J. M. (1965). Cyclotron instabilities and electromagnetic emission in the ultra low frequency and very low frequency ranges. *Journal of Geophysical Research*, **70**(1), 61–69. https://doi.org/10.1029/JZ070i001p00061

Drozdov, A. Y., Shprits, Y. Y., Usanova, M. E., Aseev, N. A., Kellerman, A. C., & Zhu, H. (2017). EMIC wave parameterization in the long-term VERB code simulation. *Journal of Geophysical Research: Space Physics*, **122**(8), 8488–8501. https://doi.org/10.1002/2017JA024389

Gurnett, D. A., & Burns, T. B. (1968). The low-frequency cutoff of ELf emissions. *Journal of Geophysical Research*, **73**(23), 7437–7445. https://doi.org/10.1029/JA073i023p07437

Gurnett, D. A. (1976). Plasma wave interactions with energetic ions near the magnetic equator. *Journal of Geophysical Research*, **81**, 2765–2770. https://doi.org/10.1029/JA081i016p02765

Hanzelka, M., Němec, F., Santolík, O., & Parrot, M. (2022). Statistical analysis of wave propagation properties of equatorial noise observed at low altitudes. *Journal of Geophysical Research: Space Physics*, **127**(7), e2022JA030416. https://doi.org/10.1029/2022JA030416

Hrbáčková, Z., Santolík, O., Němec, F., Macúšová, E., & Cornilleau-Wehrlin, N. (2015). Systematic analysis of occurrence of equatorial noise emissions using 10 years of data from the Cluster mission. *Journal of Geophysical Research: Space Physics*, **120**, 1007–1021. https://doi.org/10.1002/2014JA020268

Horne, R.B., & Thorne, R.M. (1990). Ion cyclotron absorption at the second harmonic of the oxygen gyrofrequency. *Geophysical Research Letters*, **17**(12), 2225–2228. https://doi.org/10.1029/GL017i012p02225

Horne, R. B., Wheeler, G. V., & Alleyne, H. S. C. K. (2000). Proton and electron heating by radially propagating fast magnetosonic waves. *Journal of Geophysical Research: Space Physics*, **105**, 27597–27610. https://doi.org/10.1029/2000JA000018

Horne, R. B., Thorne, R. M., Glauert, S. A., Meredith, N. P., Pokhotelov, D., & Santolík, O. (2007). Electron acceleration in the Van Allen radiation belts by fast magnetosonic waves. *Geophysical Research Letters*, **34**(17), L17107. https://doi.org/10.1029/2007GL030267

Hu, Y., & Denton, R. (2009). Two-dimensional hybrid code simulation of electromagnetic ion cyclotron waves in a dipole magnetic field. *Journal of Geophysical Research: Space Physics*, **114**(A12). https://doi.org/10.1029/2009ja014570

Hu, Y., Denton, R., & Johnson, J. R. (2010). Two-dimensional hybrid code simulation of electromagnetic ion cyclotron waves of multi-ion plasmas in a dipole magnetic field. *Journal of Geophysical Research: Space Physics*, **115**(A9). https://doi.org/10.1029/2009ja015158

Horne, R. B., & Miyoshi, Y. (2016). Propagation and linear mode conversion of magnetosonic and electromagnetic ion cyclotron waves in the radiation belts. Geophysical Research Letters, 43(19), 10034–10039. https://doi.org/10.1002/2016GL070216

Johnson, J. R., Chang, T., & Crew, G. B. (1995). A study of mode conversion in an oxygen-hydrogen plasma. *Physics of Plasmas*, **2**(4), 1274–1284. https://doi.org/10.1063/1.871339

Johnson, J. R., & Cheng, C. Z. (1999). Can ion cyclotron waves propagate to the ground?

Geophysical Research Letters, **26**(6), 671–674. https://doi.org/10.1029/1999GL900074
Jordanova, V. K., Miyoshi, Y. S., Zaharia, S., Thomsen, M. F., Reeves, G. D., Evans, D. S., et al. (2006). Kinetic simulations of ring current evolution during the Geospace Environment Modeling challenge events. *Journal of Geophysical Research: Space Physics*, **111**, A11S10. https://doi.org/10.1029/2006JA011644
Kageyama, A., Sugiyama, T., Watanabe, K., & Sato, T. (2006). A note on the dipole coordinates. *Computational Geosciences*, **32**, 265–269. https://doi.org/10.1016/j.cageo.2005.06.006
Kasahara, Y., Sawada, A., Yamamoto, M., Kimura, I., Kokubun, S., & Hayashi, K. (1992). Ion cyclotron emissions observed by the satellite Akebono in the vicinity of the magnetic equator. *Radio Science*, **27**, 347–362. https://doi.org/10.1029/91RS01872
Kasahara, Y., Kenmochi, H., & Kimura, I. (1994). Propagation characteristics of the ELF emissions observed by the satellite Akebono in the magnetic equatorial region. *Radio Science*, **29**(4), 751–767. https://doi.org/10.1029/94RS00445
Kazakov, Y. O., & Fülüp, T. (2013). Mode conversion of waves in the ion-cyclotron frequency range in magnetospheric plasmas. *Physical Review Letters*, **111**, 125002. https://doi.org/10.1103/PhysRevLett.111.125002
Khazanov, G. V., Gamayunov, K. V., Gallagher, D. L., & Kozyra, J. U. (2006), Self-consistent model of magnetospheric ring current and propagating electromagnetic ion cyclotron waves: Waves in multi-ion magnetosphere, *Journal of Geophysical Research: Space Physics*, **111**, A10202, https://doi:10.1029/2006JA011833
Khazanov, G. V., Gamayunov, K. V., Gallagher, D. L., Kozyra, J. U., & Liemohn, M. W. (2007), Self-consistent model of magnetospheric ring current and propagating electromagnetic ion cyclotron waves: 2. Wave-induced ring current precipitation and thermal electron heating, *Journal of Geophysical Research: Space Physics*, **112**, A04209, https://doi:10.1029/2006JA012033.
Kim, E.-H., & J. R. Johnson (2014), Comment on mode conversion of waves in the ion-cyclotron frequency range in magnetospheric plasmas, *Physical Review Letters*, **113**, 089501. https://doi.org/10.2172/1128922
Kim, E.-H., & Johnson, J. R. (2016). Full-wave modeling of EMIC waves near the He+ gyrofrequency. *Geophysical Research Letters*, **43**(1), 13–21. https://doi.org/10.1002/2015GL066978
Kimura, I. (1966). Effects of ions on whistler-mode ray tracing. *Radio Science*, **13**, 269–283. https://doi.org/10.1002/rds196613269
Kimura, I., Goto, Y., Katoh, K., Mochizuki, R., & Nakamoto Y. (2020). IWANE (Ray tracing program for Investigation of WAves Near the Earth) (Version 1.0) [Software]. http://space.rish.kyoto-u.ac.jp/software/IWANE_src.zip
Kozyra, J., Cravens, T., Nagy, A., Fontheim, E., & Ong, R. (1984). Effects of energetic heavy ions on electromagnetic ion cyclotron wave generation in the plasmapause region. *Journal of Geophysical Research: Space Physics*, **89**(A4), 2217– 2233. https://doi.org/10.1029/JA089iA04p02217
Laakso, H., Junginger, H., Roux, A., Schmidt, R., & de Villedary, C. (1990). Magnetosonic waves above fc(H+) at geostationary orbit: GEOS 2 results. *Journal of Geophysical Research: Space Physics*, **95**(A7), 10609–10621. https://doi.org/10.1029/JA095iA07p10609
Lee, D. H., Johnson, J. R., Kim, K., & Kim, K. S. (2008). Effects of heavy ions on ULF wave resonances near the equatorial region. *Journal of Geophysical Research: Space Physics*, **113**, A11212. https://doi.org/10.1029/2008JA013088
Li, J., Ni, B., Ma, Q., Xie, L., Pu, Z., Fu, S., et al. (2016). Formation of energetic

electron butterfly distributions by magnetosonic waves via Landau resonance. *Geophysical Research Letters*, **43**, 3009–3016. https://doi.org/10.1002/2016GL067853

Liu, K., Gary, S. P., & Winske, D. (2011). Excitation of magnetosonic waves in the terrestrial magnetosphere: Particle-in-cell simulations. *Journal of Geophysical Research: Space Physics*, **116**, A07212. https://doi.org/10.1029/2010JA016372

Liu, X., Chen, L., Yang, L., Xia, Z., & Malaspina, D. M. (2018). One-dimensional full wave simulation of equatorial magnetosonic wave propagation in an inhomogeneous magnetosphere. *Journal of Geophysical Research: Space Physics*, **123**(1), 587–599. https://doi.org/10.1002/2017JA024336

Lyons, L. R., & Thorne, R. M. (1972). Parasitic pitch angle diffusion of radiation belt particles by ion cyclotron waves. *Journal of Geophysical Research: Space Physics*, **77**(28), 5608– 5616. https://doi.org/10.1029/JA077i028p05608

Ma, Q., Li, W., Thorne, R. M., & Angelopoulos, V. (2013). Global distribution of equatorial magnetosonic waves observed by THEMIS. *Geophysical Research Letters*, **40**, 1895–1901. https://doi.org/10.1002/grl.50434

Ma, Q., Li, W., Bortnik, J., Kletzing, C. A., Kurth, W. S., Hospodarsky, G. B., & Wygant, J. R. (2019). Global survey and empirical model of fast magnetosonic waves over their full frequency range in earth's inner magnetosphere. *Journal of Geophysical Research: Space Physics*, **124**, 10270–10282. https://doi.org/10.1029/2019JA027407

Matsuda, S., Kasahara, Y., & Kletzing, C. A. (2016). Variation in crossover frequency of emic waves in plasmasphere estimated from ion cyclotron whistler waves observed by van allen probe a. *Geophysical Research Letters*, **43**(1), 28– 34. https://doi.org/10.1002/2015GL066893

Min, K., & Liu, K. (2016). Understanding the growth rate patterns of ion Bernstein instabilities driven by ring-like proton velocity distributions. *Journal of Geophysical Research: Space Physics*, **121**, 3036–3049. https://doi.org/10.1002/2016JA022524

Min, K., Němec, F., Liu, K., Denton, R. E., & Boardsen, S. A. (2019). Equatorial propagation of the magnetosonic mode across the plasmapause: 2-D PIC simulations. *Journal of Geophysical Research: Space Physics*, **124**, 4424–4444. https://doi.org/10.1029/2019ja026567

Min, K., Kim, J., Ma, Q., Jun, C.-W, & Liu, K. (2021). Unusual high frequency EMIC waves: Detailed analysis of EMIC wave excitation and energy coupling between EMIC and magnetosonic waves. *Advances in Space Research*, **69**, 35–47. https://doi.org/10.1016/j.asr.2021.07.039

Miyoshi, Y., Matsuda, S., Kurita, S., Nomura, K., Keika, K., Shoji, M., et al. (2019). EMIC waves converted from equatorial noise due to M/Q = 2 ions in the plasmasphere: Observations from Van Allen Probes and Arase. *Geophysical Research Letters*, **46**, 5662–5669. https://doi.org/10.1029/2019GL083024

Němec, F., Santolík, O., Gereová, K., Macúšová, E., de Conchy, Y., & Cornilleau-Wehrlin, N. (2005). Initial results of a survey of equatorial noise emissions observed by the cluster spacecraft. *Planetary and Space Science*, **53**(1), 291–298. https://doi.org/10.1016/j.pss.2004.09.055

Němec, F., Santolík, O., Pickett, J. S., Hrbáčková, Z., & Cornilleau-Wehrlin, N. (2013). Azimuthal directions of equatorial noise propagation determined using 10 years of data from the Cluster spacecraft. *Journal of Geophysical Research: Space Physics*, **118**, 7160–7169. https://doi.org/10.1002/2013JA019373

Němec, F., Parrot, M., & Santolík, O. (2016). Equatorial noise emissions observed by the DEMETER spacecraft during geomagnetic storms. *Journal of Geophysical Research: Space Physics*, **121**, 9744–9757. https://doi.org/10.1002/2016JA023145

Pakhotin, I. P., Mann, I. R., Sydorenko, D., & Rankin, R. (2022). Novel EMIC wave propagation pathway through Buchsbaum resonance and interhemispheric wave interference: Swarm observations and modeling. *Geophysical Research Letters*, **49**, e2022GL098249. https://doi.org/10.1029/2022GL098249

Perraut, S., Roux, A., Robert, P., Gendrin, R., Sauvaud, J.-A., Bosqued, J.-M., et al. (1982). A systematic study of ULF waves above FH+ from GEOS 1 and 2 measurements and their relationships with proton ring distributions. *Journal of Geophysical Research: Space Physics*, **87**(A8), 6219–6236. https://doi.org/10.1029/JA087iA08p06219

Perraut, S., Gendrin, R., Roux, A., & de Villedary, C. (1984). Ion cyclotron waves: Direct comparison between ground-based measurements and observations in the source region. *Journal of Geophysical Research*, **89**(A1), 195– 202. https://doi.org/10.1029/JA089iA01p00195

Pokhrel, S., Shankar, V. & Simpson, J. J. (2018). 3-D FDTD Modeling of Electromagnetic Wave Propagation in Magnetized Plasma Requiring Singular Updates to the Current Density Equation. *IEEE Transactions on Antennas and Propagation*, **66**(9), 4772-4781. doi: 10.1109/TAP.2018.2847601

Posch, J. L., Engebretson, M. J., Olson, C. N., Thaller, S. A., Breneman, A. W., Wygant, J. R., et al. (2015). Low-harmonic magnetosonic waves observed by the Van Allen Probes. *Journal of Geophysical Research: Space Physics*, **120**(8), 6230– 6257. https://doi.org/10.1002/2015JA021179

Rauch, J. L., & Roux, A. (1982). Ray tracing of ULF waves in a multicomponent magnetospheric plasma: Consequences for the generation mechanism of ion cyclotron waves. *Journal of Geophysical Research: Space Physics*, **87**(10), 8191–8198. https://doi.org/10.1029/JA087iA10p08191

Russell, C. T., Holzer, R. E., & Smith, E. J. (1970). OGO 3 observations of ELF noise in the magnetosphere: 2. The nature of the equatorial noise. *Journal of Geophysical Research*, **75**(4), 755–768. https://doi.org/10.1029/JA075i004p00755

Saikin, A. A., Zhang, J.-C., Allen, R. C., Smith, C. W., Kistler, L. M., Spence, H. E., et al. (2015). The occurrence and wave properties of H+-, He+-, and O+-band EMIC waves observed by the Van Allen Probes. *Journal of Geophysical Research: Space Physics*, **120**, 7477– 7492. https://doi.org/10.1002/2015JA021358

Saikin, A. A., Drozdov, A. Y., & Malaspina, D. M. (2022). Low frequency plasmaspheric hiss wave activity parameterized by plasmapause location: Models and simulations. *Journal of Geophysical Research: Space Physics*, **127**, e2022JA030687. https://doi.org/10.1029/2022JA030687

Sakaguchi, K., Shiokawa, K., Ieda, A., Miyoshi, Y., Otsuka, Y., Ogawa, T., et al. (2007). Simultaneous ground and satellite observations of an isolated proton arc at subauroral latitudes. *Journal of Geophysical Research: Space Physics*, **112**, A04202. https://doi.org/10.1029/2006JA012135

Santolík, O., Parrot, M., & Lefeuvre, F. (2003). Singular value decomposition methods for wave propagation analysis. *Radio Science*, **38**(1), 1010. https://doi.org/10.1029/2000RS002523

Santolík, O., Nemec, F., Gereova, K., Macusova, E., de Conchy, Y., & Cornilleau-Wehrlin, N. (2004). Systematic analysis of equatorial noise below the lower hybrid frequency. *Annales de Geophysique*, **22**(7), 2587–2595. https://doi.org/10.5194/angeo-22-2587-2004

Santolík, O., Parrot, M., & Němec, F. (2016). Propagation of equatorial noise to low altitudes: Decoupling from the magnetosonic mode. *Geophysical Research Letters*, **43**,

6694–6704. https://doi.org/10.1002/2016GL069582
Streltsov, A. V., Lampe, M., Manheimer, W., Ganguli, G., & Joyce, G. (2006). Whistler propagation in an inhomogeneous plasma. *Journal of Geophysical Research: Space Physics*, **111**, A03216. https://doi.org/10.1029/2005JA011357
Stix, T. H. (1992). Waves in plasmas. New York: AIP Press.
Sun, J., Chen, L., & Wang, X. (2020). Wave normal angle distribution of magnetosonic waves in the Earth's magnetosphere: 2D PIC simulation. *Journal of Geophysical Research: Space Physics*, **125**, e2020JA028012. https://doi.org/10.1029/2020ja028012
Swanson, D. G. (2003). Plasma Waves. Bristol and Philadelphia: Institute of Physics Publishing
Taflove, A., & Hagness, S. C. (2005). Computational electromagnetics: Finite-difference time-domain method. Norwell, MA, USA: Artech House.
Teng, S., Li, W., Tao, X., Ma, Q., Wu, Y., Capannolo, L., et al. (2019a). Generation and characteristics of unusual high frequency EMIC waves. *Geophysical Research Letters*, **46**, 14230–14238. https://doi.org/10.1029/2019GL085220
Teng, S., Li, W., Tao, X., Ma, Q., & Shen, X.-C. (2019b). Characteristics and generation of low-frequency magnetosonic waves below the proton gyrofrequency. *Geophysical Research Letters*, **46**(21), 11652–11660. https://doi.org/10.1029/2019GL085372
Thorne, R.M., & Horne, R.B. (1992). The contribution of ion-cyclotron waves to electron heating and SAR-arc excitation near the storm-time plasmapause. *Geophysical Research Letters*, **19**(4), 417–420. https://doi.org/10.1029/92GL00089
Thorne, R.M., & Horne, R.B. (1993). Cyclotron absorption of ion-cyclotron waves at the bi-ion frequency. *Geophysical Research Letters*, **20**(4), 317–320. https://doi.org/10.1029/93GL00089
Tsurutani, B. T., Falkowski, B. J., Pickett, J. S., Verkhoglyadova, O. P., Santolik, O., & Lakhina, G. S. (2014). Extremely intense ELF magnetosonic waves: A survey of polar observations. *Journal of Geophysical Research: Space Physics*, **119**, 964–977. https://doi.org/10.1002/2013JA019284
Usanova, M. E., Drozdov, A., Orlova, K., Mann, I. R., Shprits, Y., Robertson, M. T., et al. (2014). Effect of EMIC waves on relativistic and ultra-relativistic electron populations: Ground-based and Van Allen Probes observations. *Geophysical Research Letters*, **41**, 1375–1381. https://doi.org/10.1002/2013GL059024
Wu, Z., Su, Z., Liu, N., Gao, Z., Zheng, H., Wang, Y., & Wang, S. (2021). Off-equatorial source of magnetosonic waves extending above the lower hybrid resonance frequency in the inner magnetosphere. *Geophysical Research Letters*, **48**, e2020GL091830. https://doi.org/10.1029/2020GL091830
Xiao, F., Zhou, Q., He, Z., & Tang, L. (2012a). Three-dimensional ray tracing of fast magnetosonic waves. *Journal of Geophysical Research: Space Physics*, **117**, A06208. https://doi.org/10.1029/2012JA017589
Xiao, F., Yang, C., Zhou, Q., He, Z., He, Y., Zhou, X., & Tang, L. (2012b). Nonstorm time scattering of ring current protons by electromagnetic ion cyclotron waves. *Journal of Geophysical Research: Space Physics*, **117**, A08204. https://doi.org/10.1029/2012JA017922
Xiao, F., Yang, C., Su, Z., Zhou, Q., He, Z., He, Y., Baker, D. N., Spence, H. E., Funsten, H. O., & Blake, J. B. (2015a). Wave-driven butterfly distribution of Van Allen belt relativistic electrons. *Nature Communications*, **6**, 8590. https://doi.org/10.1038/ncomms9590
Xiao, F., Zhou, Q., He, Y., Yang, C., Liu, S., Baker, D. N., et al. (2015b). Penetration of magnetosonic waves into the plasmasphere observed by the Van Allen Probes.

Geophysical Research Letters, **42**, 7287–7294. https://doi.org/10.1002/2015GL065745
Xu, X., Chen, L., Zhou, C., Liu, X., Xia, Z., Simpson, J. J., & Zhang, Y. (2020a). Two-dimensional full-wave simulation of whistler mode wave propagation near the local lower hybrid resonance frequency in a dipole field. *Journal of Geophysical Research: Space Physics*, **125**(4), e2019JA027750. https://doi.org/10.1029/2019JA027750
Xu, X., Zhou, C., Chen, L., Xia, Z., Liu, X., Simpson, J. J., & Zhang, Y. (2020b). Two dimensional full-wave modeling of propagation of low-altitude hiss in the ionosphere. *Geophysical Research Letters*, **47**(4), e2019GL086601. https://doi.org/10.1029/2019GL086601
Xu, X., Zhou, C., Chen, L., & Horne, R. B. (2023). Modeling the propagation of fast magnetosonic waves and their conversion to electromagnetic ion cyclotron waves at low L shells [Dataset]. Zenodo. https://doi.org/10.5281/zenodo.7875579
Yee, K. (1966). Numerical solution of initial boundary value problems involving Maxwell's equation in isotropic media. *IEEE Transactions on Antennas and Propagation*, **14**(3), 302–307. doi: 10.1109/TAP.1966.1138693
Yu, X., Yuan, Z., Yao, F., & Ouyang, Z. (2021). Radially full reflection of fast magnetosonic waves near the cut-off frequency. *Journal of Geophysical Research: Space Physics*, **126**, e2021JA029508. https://doi.org/10.1029/2021JA029508
Zou, Z., Zuo, P., Ni, B., Wei, F., Zhao, Z., Cao, X., et al. (2019). Wave normal angle distribution of fast magnetosonic waves: A survey of Van Allen Probes EMFISIS observations. *Journal of Geophysical Research: Space Physics*, **124**, 5663–5674. https://doi.org/10.1029/2019JA026556
Zhang, Z., Xiang, Z., Wang, Y., Ni, B., & Li, X. (2021). Electron acceleration by magnetosonic waves in the deep inner belt (L = 1.5–2) region during geomagnetic storm of August 2018. *Journal of Geophysical Research: Space Physics*, **126**, e2021JA029797. https://doi.org/10.1029/2021JA02979
Zhang, J., Halford, A. J., Saikin, A. A., Huang, C. L., Spence, H. E., Larsen, B. A., et al. (2016). EMIC waves and associated relativistic electron precipitation on 25–26 January 2013. *Journal of Geophysical Research: Space Physics*, **121**, 11086–11100. https://doi.org/10.1002/2016JA022918
Zhima, Z., Chen, L., Fu, H., Cao, J., Horne, R. B., & Reeves, G. (2015). Observations of discrete magnetosonic waves off the magnetic equator. *Geophysical Research Letters*, **42**(22), 9694–9701. https://doi.org/10.1002/2015GL066255
Zhou, R., Ni, B., Fu, S., Teng, S.,Tao, X., Hu, Z., et al. (2022). Global distribution of concurrent EMIC waves and magnetosonic waves: A survey of Van Allen Probes observations. *Journal of Geophysical Research: Space Physics*, **127**, e2021JA030093. https://doi.org/10.1029/2021JA030093